# A Model-Based Probabilistic Inversion Framework for Characterizing Wire Fault Detection Using TDR

Stefan Schuet, *Member, IEEE,* Doğan Timuçin, and Kevin Wheeler, *Senior Member, IEEE*

***Abstract*—Time-domain reflectometry (TDR) is one of the standard methods for diagnosing faults in electrical wiring and interconnect systems, with a long-standing history focused mainly on hardware development of both high-fidelity systems for laboratory use and portable hand-held devices for field deployment. While these devices can easily assess distance to hard faults such as sustained opens or shorts, their ability to assess subtle but important degradation such as chafing remains an open question. This paper presents a unified framework for TDR-based chafing fault detection in lossy coaxial cables by combining an $S$-parameter based forward modeling approach with a probabilistic (Bayesian) inference algorithm. Results are presented for the estimation of nominal and faulty cable parameters from laboratory data.**

***Index Terms*—Bayesian, fault detection, $S$-parameters, time-domain reflectometry (TDR), wiring.**

## I. Introduction

THE Federal Aviation Administration (FAA), Naval Systems Air Command (NAVAIR) and National Aeronautics and Space Administration (NASA) have all identified wire chafing as the largest factor contributing to electrical wiring and interconnect system failures in aging aircraft [1]. Furthermore, the detection of wire chafing is important because it leads to more significant problems such as opens and shorts. This article provides a technically extended discussion of results initially published in [2] on a new general method for characterizing wiring chafe detectability using time-domain reflectometry (TDR). Our approach combines physics-based modeling of signal propagation through a faulty cable within a TDR setup, with a probabilistic inference method for recovering key system parameters, including fault location and size, from measured data. The method further provides clear uncertainty information regarding the estimated parameters, without relying on linear model approximation techniques. Finally, it is flexible enough to apply to a variety of wiring types, measurement conditions, and arbitrary input interrogation signals.

TDR is an industry-standard method for diagnosing faults in wiring systems. Intuitively, it works by applying an input signal (*e.g.*, step, Gaussian pulse, pseudo-noise, *etc.*) to the wire under test, which propagates as a wave along the line. When the main wavefront passes over a fault on the line, part of it is reflected and travels back to the input where it can be measured. Finally, the measured response is diagnosed, either by eye or using automated software, for signal variation caused by potential faults.

Wiring fault detection using TDR has a long history, where the detection of chafing is considered significantly more difficult than hard failures such as opens and shorts [3]. Over the last decade, many time-domain reflectometry (TDR), frequency-domain reflectometry (FDR) and time- and frequency-based investigations were published [3]–[9]. Among these investigations and many others, the primary mechanism for automated fault detection is the application of a sliding correlator, or matched filter, to detect fault location. In addition, knowledge of the wire material parameters such as permittivity and conductivity along with measurement setup and impedance matching conditions are usually either assumed known in advance, or fixed from baseline measurements.

Unfortunately, correlation methods generally fail to detect small faults in practice for at least a couple of reasons. First, when baseline measurements are available, they are often unreliable because of the continuously changing cable characteristics and measurement conditions in the field. Second, matched-filter based techniques only provide relative information regarding fault severity in terms of the amplitude of the fault signature, and its location in time. Translating that information into the *physical* fault geometry and its distance from the source again depends on foreknowledge of the channel properties. For the wire fault detection problem however, the channel depends not only on the same changes in cable characteristics and measurement conditions that affect the baseline, but also on the location of the fault itself. Even high-quality cable exhibits loss and dispersion effects that appreciably change the shape of the propagating signal wave as a function of the propagation distance. In essence, one does not reliably know ahead of time the correct matched-filter to use. Finally, because correlation-based detection methods fail to accurately account for these effects, they can not be used to reliably answer basic trade-space analysis questions such as fault detectability versus distance.

The method presented in this article overcomes the difficulties with traditional approaches highlighted in the previous paragraph. We begin in section II by developing a framework based on *scattering parameters* (or $S$-parameters) to build a computationally efficient yet accurate forward model for how chafed shielding affects signal propagation, and thus the measured TDR response. This model includes the key physical parameters contributing to signal loss and dispersion effects such as dielectric permittivity, finite metallic conductivity, and source–cable impedance mismatch. In section III, this forward model is then combined with a general Bayesian probabilistic

The authors are with NASA Ames Research Center, Moffett Field, CA, 94035 USA (e-mail: stefan.r.schuet@nasa.gov).

Final draft published in the IEEE Transactions on Instrumentation an Measurement, Vol. 60, No. 5, May 2011.

inversion procedure, which enables robust fault parameter estimation in the presence of measurement noise and initial model parameter uncertainty (*i.e.*, uncertainty in permittivity, conductivity, impedance mismatch, *etc.*). In fact, this method simultaneously estimates not only fault location and size, but an entire set of key parameters affecting the measured TDR response along with the corresponding joint uncertainty information, which in turn enables a reliable characterization of trade-space issues. Finally, in section IV, example results characterizing fault detectability in RG58 coaxial cable are presented. In summary, our approach combines a physics-based model with a Bayesian probabilistic inversion method; and this approach has found success in other TDR applications, for example see [10], as well as in *many* other fields.

To keep the presentation clear and concrete, our method is explained in terms of a simple example involving a single chafing fault in coaxial cable. However, it should be clear throughout that this example is easily generalized to handle a wide variety of wire types and fault conditions, simply by substituting the appropriate $S$-parameter models for the particular types of cable and fault under investigation. In addition, a new effective TDR hardware model is derived that may be common to many systems.

Finally, before moving on, we admit up front that the fault parameter retrieval method presented here is not well suited for practical application in the field, because it is computationally too expensive and hence slow (at the present time). However, the method is important because it enables a general characterization of fault detectability in a wide variety of wiring systems using virtually any TDR hardware measurement setup and input interrogation signal. As such, the approach presented here can be used to establish fundamental limits on fault detection performance in advance of further hardware and software development cost.

## II. Forward Model for TDR

This section describes our systematic approach to building a computationally efficient forward model for the interrogation of a chafed coaxial cable using TDR. The modeling method of choice is the $S$-parameter formalism; the reader is referred to [11], [12] for a refresher. Specifically, each cable segment is treated as a two-port device with a $2 \times 2$ matrix of $S$-parameters. These $S$-parameters are then combined in cascade to obtain the overall response of the system. In this process, one is aided by the formula

$$\Gamma_1 = S_{11} + \frac{S_{12}S_{21}\Gamma_2}{1 - S_{22}\Gamma_2}, \tag{1}$$

which relates the reflection coefficients seen looking into port 1 ($\Gamma_1$) and out of port 2 ($\Gamma_2$) of a two-port device within a network.

### A. Coaxial Cable

For nominal (*i.e.*, unfaulted) segments of the cable, one has

$$\begin{aligned} S_{11} = S_{22} &= 0, \\ S_{12} = S_{21} &\equiv S_0(l), \end{aligned}$$

where the dependence of the relevant $S$-parameters on the cable length $l$ has been indicated explicitly for later convenience. Adopting the standard textbook model for a coaxial transmission line (see, for instance, [13], p. 551) one obtains

$$S_0(l) = e^{-jk(\omega)l}, \tag{2}$$

where

$$k(\omega) \simeq \omega\sqrt{\mu_0\epsilon_d} + \frac{1}{2\ln(b/a)}\sqrt{\frac{\omega\epsilon_d}{j\sigma_c}}\left(\frac{1}{a} + \frac{1}{b}\right). \tag{3}$$

In (3), $a$ and $b$ respectively denote the radius of the core and the (inner) radius of the shield, both of which are assumed to have a (finite) conductivity $\sigma_c$, while $\epsilon_d$ denotes the permittivity of the insulator separating the two conductors, and $\mu_0$ is the vacuum permeability. We will also need the characteristic impedance of the cable, which is given by

$$Z_0 = \frac{\ln(b/a)}{2\pi}\,\frac{k(\omega)}{\omega\epsilon_d}. \tag{4}$$

The above formulation relates the key cable parameters ($S_0$ and $Z_0$) directly to the "constitutive" parameters ($\sigma_c$ and $\epsilon_d$), and is therefore preferable to the distributed RLCG parameter model that is more commonly found in textbook treatments. Finally, with this model and all that follows it is assumed that the material resonances of the insulator lie well above the frequency range of interest (say, DC to 10 GHz), and therefore the permittivity is taken to be a real-valued constant. Thus, the attenuation and dispersion of signals along the cable are due solely to the finite conductivity of the core and shield. One could, of course, employ a suitable complex-valued, frequency-dependent parametric model for the permittivity, should the dielectric loss be deemed necessary to include in the model.

### B. Impedance Step

In this section, a model for an impedance step in the system is derived. Figure 1 illustrates the problem in a generic setting. The task is to determine $\Gamma_1$ given $\Gamma_2$, $Z_2$, and $Z_1$. First, we define the reflection coefficient caused by the impedance step (for waves moving to the right):

$$\Gamma_s = \frac{Z_2 - Z_1}{Z_1 + Z_2} = \left[\frac{V_1^-}{V_1^+}\right]_{V_2^- = 0}.$$

Using a voltage loop, it is easy to see that the transmission coefficient must then be $1+\Gamma_s$. Combining these two facts, we can write the following two equations for the voltage waves entering and exiting the impedance step:

$$\begin{aligned} V_1^- &= \Gamma_s V_1^+ + (1-\Gamma_s)V_2^-, \\ V_2^+ &= (1+\Gamma_s)V_1^+ - \Gamma_s V_2^-, \end{aligned}$$

and from these two equations, the desired result is easily obtained:

$$\Gamma_1 = \frac{\Gamma_s + \Gamma_2}{1 + \Gamma_s\Gamma_2}. \tag{5}$$

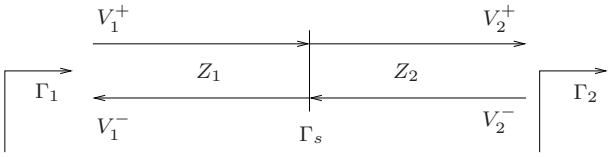


Fig. 1. Impedance step.

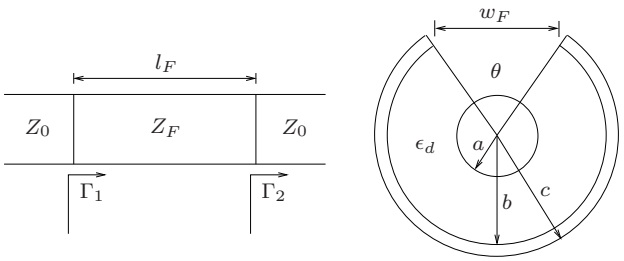


Fig. 2. (Left) A constant-impedance model for a chafed cable segment. (Right) Cross-section of a chafed coaxial cable.

### C. Chafe Fault

A simple yet accurate model for the $S$-parameters of a chafed coaxial cable is now presented using an approach that is generalizable to other types of wiring. The situation of interest is depicted in Figure 2, where a segment of length $l_F$ and width $w_F$ is chafed on a coaxial cable with characteristic impedance $Z_0$. The chafed segment is modeled as having a constant (*i.e.*, $z$- and $\omega$-independent) characteristic impedance $Z_F$.

To derive $S_{11}$ of the chafe, we conceptually match the coaxial cable impedance on the right, and define

$$\Gamma_2 = \frac{Z_0 - Z_F}{Z_0 + Z_F}$$

as the reflection coefficient for a wave traveling into the second impedance discontinuity. Any wave transmitted through this discontinuity will never return because the impedance is matched. Now, if we move $l_F$ meters to the left of the second impedance discontinuity to a position just after the first impedance discontinuity the input reflection coefficient will be

$$\Gamma_2 e^{-j2\omega t_d},$$

where $t_d$ is the one-way travel time from the first to the second discontinuity (*i.e.*, $2t_d$ seconds pass as the incident wave travels this distance, reflects from the second discontinuity, and travels back). Clearly, $t_d = l_F/v_p$, where $v_p$ is the wave propagation velocity inside the fault. The only remaining step is to cross the first impedance discontinuity. To do this, we use equation (5) from §II-B, where $\Gamma_s = -\Gamma_2$. Thus,

$$S_{11} = \Gamma_1 = \frac{\Gamma_2(e^{-j2\omega t_d} - 1)}{1 - \Gamma_2^2 e^{-j2\omega t_d}}, \tag{6}$$

where the first equality follows because the output impedance is matched.

Next, we derive an approximation for $S_{21}$ by simply noting that $(1 - \Gamma_2)$ times the incident voltage wave is transmitted through the first impedance discontinuity, delayed by $t_d$, and $(1+\Gamma_2)$ is transmitted through the second discontinuity. Thus,

$$S_{21} \approx (1 - \Gamma_2^2)e^{-j\omega t_d}. \tag{7}$$

This is an approximation because there are additional reflections that ring within the fault.

The exact expression is derived by tracing the voltage waves as they reflect within the fault, and adding the transmitted parts of the delayed reflections together in an infinite series. This procedure produces

$$S_{21} = \frac{(1 - \Gamma_2^2)e^{-j\omega t_d}}{1 - \Gamma_2^2 e^{-j2\omega t_d}}. \tag{8}$$

Note, this exact expression does produce noticeably better results when the fault magnitudes are also small (and they usually are). Finally, since this chafe model is symmetric, we have $S_{11} = S_{22}$, and $S_{21} = S_{12}$.

We must next relate the hitherto unknown parameters $Z_F$ and $v_p$ to the geometry of the chafe's cross-section shown in Figure 2. This geometry depends on the conductor radius $a$, inside shield radius $b$, and outside shield radius $c$, which are considered known for the cable under investigation. The fault impedance $Z_F$ and velocity of propagation $v_p$ are both functions of principally the chafe width $w_F$ and dielectric permittivity $\epsilon_d$. These functions are determined numerically by building lookup tables using a standard finite-difference method to solve for $Z_F$ and $v_p$ over a grid of different values for $w_F$ and $\epsilon_d$. The theoretical underpinnings and the numerical implementation of this approach are presented in [14].[1] We have found that this simple rectangular chafe geometry and lookup-table based approach are remarkably accurate for modeling practical chafes, which are typically elliptical in shape.

### D. Source Connection

In this subsection, a simple source connection model is derived. The situation is presented in Figure 3. Using the definitions shown on the schematic and a little algebra, it is easy to show that

$$\frac{V^-}{V_S} = \frac{Z_0\Gamma}{Z_0(1+\Gamma) + Z_S(1-\Gamma)}, \tag{9}$$

$$\frac{V}{V_S} = \left(\frac{1+\Gamma}{\Gamma}\right)\frac{V^-}{V_S} = \frac{Z_0(1+\Gamma)}{Z_0(1+\Gamma) + Z_S(1-\Gamma)}. \tag{10}$$

An important subtlety is that the net voltage $V$ is measured in the characteristic impedance $Z_0$, *after* any possible impedance mismatch with the source. Since most TDR systems measure voltage with respect to the source impedance rather than the line impedance, this important case is treated in the next section.

### E. TDR Hardware

A general model for the TDR hardware is shown in Figure 4. In this figure, the "down-stream network" represents any wiring system that is defined by a characteristic impedance $Z_0$ and a reflection coefficient $\Gamma_0$ at the system input. The

[1]The method presented in [14] assumes that $v_p$ is equal to the nominal velocity of propagation on the cable, which is $\simeq 1/\sqrt{\mu_0\epsilon_d}$. While this is *not* theoretically true, the assumption seems to work reasonably well in practice for the small chafe faults considered in this paper.

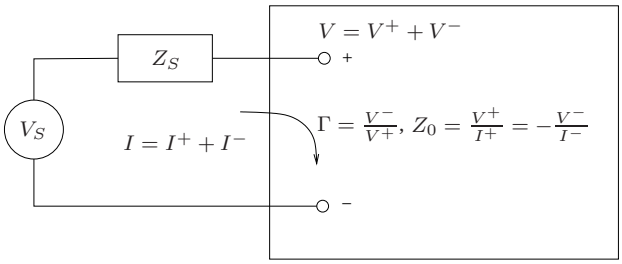


Fig. 3. Source connection.

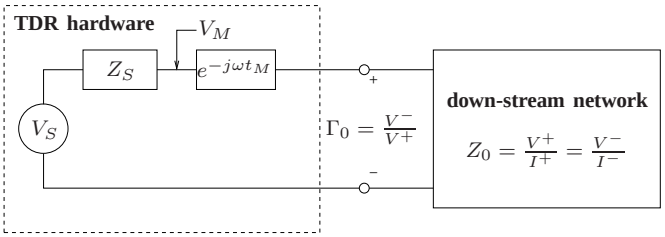


Fig. 4. TDR hardware model.

goal is to determine the experimentally measured voltage $V_M$ in terms of the TDR source voltage $V_S$.

Good models for TDR hardware should incorporate three practical effects: (1) the frequency-dependent impedance mismatch between the source and the cable, (2) a measurement delay time needed to account for signal propagation *within* the TDR unit, and (3) a gain factor to account for a typically small mis-calibration between the modeled and measured TDR response voltages. The equation below for the net transfer function captures these effects:

$$H(\omega) = \frac{V_M}{V_S} = \frac{G}{2}\left(1 + \frac{\Gamma_S + \Gamma_0}{1 + \Gamma_S\Gamma_0} e^{-j2\omega t_M}\right), \qquad (11)$$

where $\Gamma_S = (Z_0 - Z_S)/(Z_0 + Z_S)$ accounts for the port impedance mismatch, $t_M$ represents the one-way internal delay, and $G$ is the gain factor used to account for possible calibration issues. The key parameters for the TDR unit are thus seen to be the source impedance $Z_S$, the internal delay $t_M$, and the gain factor $G$.

Equation (11) is derived by processing the schematic of Figure 4 from right to left. To start, we need to deal with the fact that $\Gamma_0$ is specified with reference to $Z_0$, while the TDR voltage measurement is made with respect to $Z_S$. In other words, there is a possible impedance mismatch between the TDR port and the downstream network. This is easily accomplished by using the impedance step model presented earlier with $\Gamma_S = (Z_0 - Z_S)/(Z_0 + Z_S)$. The updated reflection transfer function after the impedance step is then

$$\Gamma_0' = \frac{\Gamma_S + \Gamma_0}{1 + \Gamma_S\Gamma_0}. \qquad (12)$$

The next step is to incorporate the delay block, which represents a time lag between the voltage measurement and the TDR port. This is also easy to do using the fact that a delay in time is equivalent to the following in the frequency domain:

$$\Gamma_M = \Gamma_0' e^{-j\omega 2t_M}. \qquad (13)$$

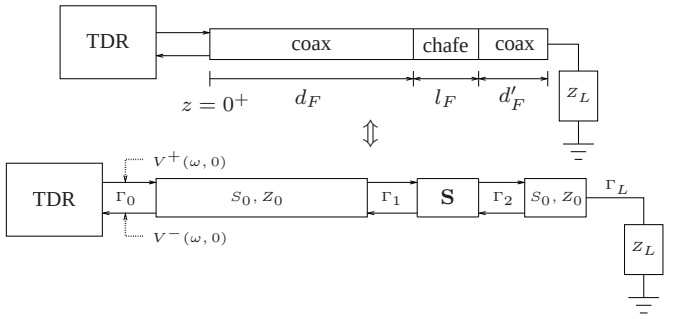


Fig. 5. $S$-parameter representation of a chafed coaxial cable.

Finally, we need to convert $\Gamma_M$, which specifies the transfer function between the forward and reverse voltage waves, into the transfer function between the net source signal $V_S$ and the measured net response signal $V_M$. With respect to Figure 3, $\Gamma$ is the reflection coefficient looking into the characteristic impedance $Z_0$. Since equation (12) already took care of the TDR port impedance mismatch, $\Gamma_M$ is looking into $Z_S$, so we can set $Z_0 = Z_S$ for this final step in our development of the TDR hardware model. Thus equation (10) above simplifies to

$$\frac{V_M}{V_S} = \frac{G}{2}(1 + \Gamma_M), \qquad (14)$$

after also multiplying the system gain factor $G$. Combining equations (12), (13), and (14) produces the TDR hardware model given by (11).

### *F. Model Synthesis*

The pieces discussed separately above are now put together to obtain the system model shown in Figure 5. The model is analyzed from right to left, starting with the load reflection coefficient $\Gamma_L = (Z_L - Z_0)/(Z_L + Z_0)$. By repeated application of equation (1), we obtain

$$\Gamma_2 = S_0^2(d_F')\Gamma_L, \qquad (15)$$

$$\Gamma_1 = S_{11} + \frac{S_{12}S_{21}\Gamma_2}{1 - S_{22}\Gamma_2}, \qquad (16)$$

$$\Gamma_0 = S_0^2(d_F)\Gamma_1, \qquad (17)$$

where $S_0(l)$ is given in (2), and $S_{ij}$ are given in (6) and (8).

Inserting these equations into (11), we obtain an *analytical* relationship between the TDR input and output signals, which explicitly contains the various physical system and fault parameters discussed above. (The derivation is straightforward, but the result is too unwieldy to include here.) Rewriting (11) in the time domain, we have

$$v_M(t) = \int_0^t h(t - t'; \theta)\, v_S(t')\, \mathrm{d}t', \qquad (18)$$

where the dependence of the impulse response $h$ on the set $\theta$ of key model parameters has been indicated to motivate the discussion in §III.

Typically, equation (18) is computed numerically using the Fast Fourier Transform algorithm. Explicitly, given a set of time samples $t_k = k\Delta t$ for $k = 0, 1, \ldots, n-1$ ($n$ odd),

where $\Delta t$ is the sampling period, the corresponding continuous frequencies are given by:

$$\omega_k = \begin{cases} \frac{2\pi k}{n\Delta t} & \text{for } k = 0, 1, \ldots, (n-1)/2; \\ -\frac{2\pi(n-k)}{n\Delta t} & \text{for } k = (n+1)/2, \ldots, n-1. \end{cases} \quad (19)$$

Thus, if we assign the $n$-dimensional vectors,

$$v_M = [v_M(t_0), v_M(t_1), \ldots, v_M(t_{n-1})]^T \quad (20)$$

$$v_S = [v_S(t_0), v_S(t_1), \ldots, v_S(t_{n-1})]^T \quad (21)$$

$$H(\theta) = [H(\omega_0, \theta), H(\omega_1, \theta), \ldots, H(\omega_{n-1}, \theta)]^T, \quad (22)$$

then,

$$v_M(\theta) = \texttt{ifft}(H(\theta) \odot \texttt{fft}(v_S)), \quad (23)$$

where we have used $\odot$ to represent an element-by-element vector multiply operation, $H(\omega, \theta)$ refers to equation (11) evaluated at a particular set of model parameters $\theta$, and of course `fft` and `ifft` represent the Fast Fourier Transform algorithm and its inverse, respectively. The computation is valid when the actual source signal is $n\Delta t$-periodic and well approximated by the sum of $n$ sinusoids with the angular frequencies $\omega_k$ given in (19) above.

Finally, we note in passing that this modeling approach can be generalized readily to a cable with chafes (or other kinds of faults) at multiple locations, and in fact to arbitrary wiring networks. Most importantly, as the number of wiring and interconnect components grows, the computational effort needed to evaluate the model grows only linearly, and the memory resources needed stays roughly *fixed*.

### *G. Full S-parameter Model for an Arbitrary Cable with Fault*

In the previous subsection, we showed how to derive the frequency-dependent input reflection coefficient for a coaxial cable with a chafe fault within a TDR setup featuring a source–cable impedance discontinuity. In this section, we derive the full $S$-parameter model for an arbitrary cable type (supporting a single mode of propagation) and with a generic fault, which can be used in analyzing other types of measurements (*e.g.*, time-domain transmissometry) as well.

Let us begin with the setup shown in Figure 6, which depicts a fault with two sections of possibly lossy cable attached to it. To derive the $S$-parameters for this faulty cable, the chain scattering matrix approach is used [12]. With this approach, the chain scattering matrix $\mathbf{T}$ for the faulty cable is readily specified as

$$\mathbf{T} = \begin{bmatrix} (A_{21}F_{21}B_{21})^{-1} & -A_{21}^{-1}F_{22}B_{21}F_{21}^{-1} \\ A_{21}F_{22}B_{21}^{-1}F_{21}^{-1} & A_{21}B_{21}(F_{21}^2 - F_{22}^2)F_{21}^{-1} \end{bmatrix},$$

where $A_{mn}$, $F_{mn}$, and $B_{mn}$ are the $S$-parameters for the first section of cable, the fault, and the second section of cable, respectively.[2] Converting the chain scattering parameters back to $S$-parameters, we get

$$\mathbf{S} = \begin{bmatrix} A_{21}^2F_{22} & A_{21}F_{21}B_{21} \\ A_{21}F_{21}B_{21} & F_{22}B_{21}^2 \end{bmatrix}. \quad (24)$$

[2]For a coaxial cable with a chafe fault, the matrices $\mathbf{A}$, $\mathbf{B}$, and $\mathbf{F}$ are to be constructed with the $S$-parameters $S_0$, $S_{11}$, and $S_{21}$ derived earlier.

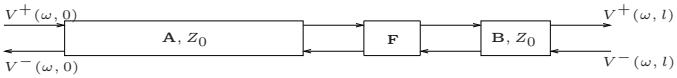


Fig. 6. Block diagram of an arbitrary cable with fault.

Now that we have the $S$-parameters for the faulty cable, the next step is to extend the formalism to include the source and the load impedance discontinuities. The situation is shown in Figure 7. The $S$-parameters for the system inside the impedance discontinuities are via:

$$\begin{aligned} b_1 &= S_{11}a_1 + S_{12}a_2, \\ b_2 &= S_{21}a_1 + S_{22}a_2, \end{aligned} \quad (25)$$

where $S_{ij}$ are given in (24). The goal now is to derive the $S$-matrix $\overline{\mathbf{S}}$ for the extended system, which is defined by the equations:

$$\begin{aligned} \overline{b}_1 &= \overline{S}_{11}\overline{a}_1 + \overline{S}_{12}\overline{a}_2, \\ \overline{b}_2 &= \overline{S}_{21}\overline{a}_1 + \overline{S}_{22}\overline{a}_2, \end{aligned}$$

given we know the $S$-parameters for the faulty cable and all the characteristic impedances $Z_0$, $Z_1$, and $Z_2$. To do this, we refer to Figure 1 and make use of the following boundary conditions (already derived in §II-B) for the voltage waves traveling into and out of the impedance discontinuities on both sides of the faulty cable:

$$\begin{aligned} a_1 &= (1+\Gamma_1)\overline{a}_1 - \Gamma_1 b_1, \quad a_2 = (1-\Gamma_2)\overline{a}_2 + \Gamma_2 b_2, \\ \overline{b}_1 &= (1-\Gamma_1)b_1 + \Gamma_1\overline{a}_1, \quad \overline{b}_2 = (1+\Gamma_2)b_2 - \Gamma_2\overline{a}_2. \end{aligned} \quad (26)$$

To solve for the $S$-parameters of the extended system, we start by solving equations (26) for $a_1$, $a_2$, $b_1$, and $b_2$ in terms of $\overline{a}_1$, $\overline{a}_2$, $\overline{b}_1$, and $\overline{b}_2$. Next, these results are substituted into equations (25), which are then solved for the elements of the matrix $\overline{\mathbf{S}}$, obtaining:

$$\overline{S}_{11} = \frac{S_{11} + \Gamma_1 - \Gamma_1\Gamma_2 S_{22} - (S_{11}S_{22} - S_{12}S_{21})\Gamma_2}{1 + S_{11}\Gamma_1 - S_{22}\Gamma_2 - (S_{11}S_{22} - S_{12}S_{21})\Gamma_1\Gamma_2} \quad (27)$$

$$\overline{S}_{12} = \frac{S_{12}(1-\Gamma_1)(1-\Gamma_2)}{1 + S_{11}\Gamma_1 - S_{22}\Gamma_2 - (S_{11}S_{22} - S_{12}S_{21})\Gamma_1\Gamma_2} \quad (28)$$

$$\overline{S}_{21} = \frac{S_{21}(1+\Gamma_1)(1+\Gamma_2)}{1 + S_{11}\Gamma_1 - S_{22}\Gamma_2 - (S_{11}S_{22} - S_{12}S_{21})\Gamma_1\Gamma_2} \quad (29)$$

$$\overline{S}_{22} = \frac{S_{22} - \Gamma_2 - \Gamma_1\Gamma_2 S_{11} + (S_{11}S_{22} - S_{12}S_{21})\Gamma_1}{1 + S_{11}\Gamma_1 - S_{22}\Gamma_2 - (S_{11}S_{22} - S_{12}S_{21})\Gamma_1\Gamma_2} \quad (30)$$

To verify the equation for $\overline{S}_{11}$, consider the case where $\Gamma_2 = \Gamma_L$ and $\Gamma_1 = 0$. After substituting these values, equation (27) becomes

$$\overline{S}_{11} = S_{11} + \frac{S_{12}S_{21}\Gamma_L}{1 - S_{22}\Gamma_L},$$

which is the same as equation (1) for the input reflection coefficient given load impedance $Z_L$ and matched source impedance (as it should be).

Use of the matrix $\overline{\mathbf{S}}$ makes it easy to derive the input/output voltage relationships with mismatched source and load impedances. This case occurs frequently in practice whenever the wire impedance mismatches the source impedance.

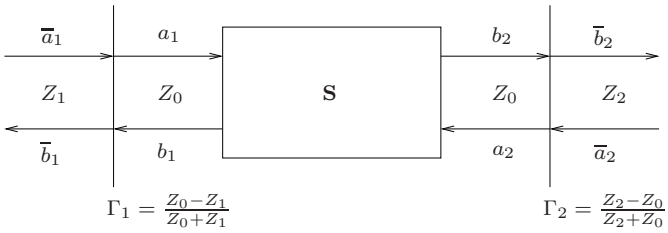


Fig. 7. Block diagram of a faulty cable attached to a source and a load.

Since the mismatch is now taken care of *within* the $S$-parameter block we can consider attaching the source and load to *matched* impedances. This means we can simply write:

$$\begin{aligned} V^+(0) &= \frac{1}{2} V_S \ \text{(since } Z_1 = Z_S\text{)} \\ V(0) &= V^+(0) + V^-(0) = \frac{1}{2}(1 + \overline{S}_{11}) V_S \\ V^-(l) &= 0 \ \text{(since } Z_2 = Z_L\text{)} \\ V(l) &= V^+(l) + V^-(l) = \frac{1}{2} \overline{S}_{21} V_S. \end{aligned}$$

## III. Probabilistic Inversion

### A. Bayesian Framework

In this section, a probabilistic framework is presented for inferring the fault parameters from measured TDR data. Starting with a sampled version of (18), the measurement process is modeled in the usual way as

$$y = v_M(\theta) + \nu, \tag{31}$$

where $v_M \in \mathbf{R}^n$ is the discrete modeled TDR response defined by equation (20), and calculated as a function of the model parameters $\theta$ (and source interrogation signal $v_S$) using equation (23); $\nu \in \mathbf{R}^n$ is a vector of additive random measurement noise; and $y \in \mathbf{R}^n$ is the time series of voltage samples forming the measured TDR signal.

Two probability distributions functions (pdfs) are now introduced for the construction of a Bayesian inversion framework: (1) the *prior* distribution $\mathbf{Pr}(\theta)$, which describes our state of knowledge regarding the unknown model parameters before any measurements are made, and (2) the *likelihood* distribution $\mathbf{Pr}(y|\theta)$, which specifies the probability of observing a particular measurement for a given set of model parameters. Bayes' theorem then gives the *posterior* distribution for $\theta$ in the form [15]

$$\mathbf{Pr}(\theta|y) = \frac{\mathbf{Pr}(y|\theta)\,\mathbf{Pr}(\theta)}{\int \mathbf{Pr}(y|\theta')\,\mathbf{Pr}(\theta')\,d\theta'}. \tag{32}$$

The maximum *a posteriori* estimate $\theta^*$ is found by solving the optimization problem

$$\text{maximize } \mathbf{Pr}(\theta|y). \tag{33}$$

Furthermore, the shape of the posterior distribution around $\theta^*$ indicates how confident we are in this estimate. There are two typical approaches to quantifying the uncertainty represented by a general distribution like $\mathbf{Pr}(\theta|y)$, which depends heavily on the nonlinear forward model (among other things). The first is to assume the distribution is approximately Gaussian around the optimal estimate $\theta^*$, and to use the inverse of the Hessian of $-\log \mathbf{Pr}(\theta^*|y)$ as an approximation for the covariance matrix, which quantifies the spread of the distribution [15, Ch. 3]. The second approach relies on the remarkable fact that one can sample random vectors directly from the posterior distribution $\mathbf{Pr}(\theta|y)$, and use a suitable measure of sample scatter to quantify the spread of the distribution, without making any additional Gaussian assumptions. This (more general) latter approach is taken up in the next subsection.

### B. Markov-Chain Monte Carlo Estimation

Finding the optimal estimate and quantifying the uncertainty associated with it are computationally challenging tasks when the forward model $v_M(\theta)$ is nonlinear in $\theta$, as in the present case. Furthermore, in cases where the forward model is an algorithm (rather than a closed-form expression), it can be prohibitively expensive to compute the gradient and the Hessian of the cost function, which are needed to solve the optimization problem (33) using traditional methods. Thus, a natural approach for this type of problem is the application of Markov-Chain Monte Carlo (MCMC) methods to obtain a set of random samples drawn directly from the posterior distribution, which are used to estimate the desired quantities by applying the law of large numbers. The underlying premise for this approach is that, for sufficiently large $N$, a set of samples

$$\theta_k \sim \mathbf{Pr}(\theta|y), \quad k = 1, 2, \ldots, N, \tag{34}$$

adequately captures the essential features of the posterior distribution. Specifically, the sample $\theta_k$ that maximizes the posterior distribution provides us with a globally optimal estimate, while the spread of the $N$ samples around $\theta_k$ may be taken as a measure of our uncertainty about this estimate. More generally, the law of large numbers guarantees that

$$\frac{1}{N} \sum_{k=1}^{N} f(\theta_k) \to \mathbf{E}[f(\theta)] = \int f(\theta)\,\mathbf{Pr}(\theta|y)\,d\theta \tag{35}$$

as $N \to \infty$. Thus, the samples can be used to estimate the expected value of almost any function of $\theta$. Standard examples are the mean $f(\theta) = \theta$ and the variance $f(\theta) = (\theta - \mathbf{E}[\theta])^2$.

There are many different MCMC-based algorithms one can implement to achieve the above sampling. The results presented in §IV were obtained using a relatively new method called *nested sampling*. This algorithm is a natural fit for solving the estimation problem posed in (33), while also estimating other relevant quantities such as the integral in the denominator of (32), which does not influence the solution of (33) but can be used for model selection (*i.e.*, choosing the best among competing forward-modeling schemes). A basic summary of the nested sampling algorithm along with a few key references are included in the appendix.

## IV. Results

This section presents a couple of example results on system parameter estimation and chafing fault detection for a 7-m long RG58 coaxial cable with an open load condition (*i.e.*, $Z_L = \infty$), along with a simulated result highlighting the

more complex nature of detecting particularly small faults. Like many other MCMC methods, nested sampling also tends to be slow: it took around 8-10 hours to solve the estimation examples discussed below on a 32-bit 1.8-GHz Linux PC.

### A. Problem Setup

Laboratory measurements were obtained using an Agilent 54754A digital TDR unit, which applies a $0.4$ V, $40$ ps rise time, step signal to the line. The elements of the measurement noise vector $\nu$ were assumed to be independent and identically distributed Gaussian random variables with zero mean and a standard deviation of $\sigma_M = 0.5$ mV, a value roughly equal to the residual error standard deviation between the measured data and the optimal model fit. Under these assumptions, the likelihood distribution is

$$\mathbf{Pr}(y|\theta) = (2\pi\sigma_M^2)^{-n/2} \exp\left\{-\frac{1}{2\sigma_M}\|y - v_M(\theta)\|^2\right\}, \tag{36}$$

where $\theta = (l, d_F, l_F, w_F, \epsilon_d, \sigma_c, Z_S, t_M, G)$ is our vector of key model parameters, all of which were carefully defined throughout section II[3].

The prior information is summarized in Table I, where $\mathcal{U}(x, y)$ denotes the uniform distribution on the interval $[x, y]$, and $\mathcal{N}^+(\mu, \sigma)$ denotes the normal distribution restricted to nonnegative values,[4] with pdf

$$f_X(x) = \begin{cases} \frac{e^{-(x-\mu)/2\sigma^2}}{\Phi(\mu/\sigma)\sqrt{2\pi\sigma^2}}, & x \geq 0 \\ 0, & \text{otherwise} \end{cases}, \tag{37}$$

where $\Phi(z) = [1 + \mathrm{erf}(z/\sqrt{2})]/2$ represents the cumulative distribution function of a standard normal random variable. This prior specification represents information and uncertainty regarding the cable material properties and TDR equipment specifications in a *reasonable* way. For example, the nominal values of $\sigma_c$ and $\epsilon_d$ are typically supplied by the cable manufacturer, but the parameters of a *particular* cable may deviate appreciably from the "batch" values, a fact captured by the specified prior probability distributions; the same argument holds for the TDR hardware parameters as well.

Before any measurements are made, our prior knowledge of each key parameter is assumed independent of the other parameters, except for the distance to fault $d_F$ and cable length $l$, which are jointly distributed according to

$$\mathbf{Pr}(d_F, l) = \mathbf{Pr}(d_F|l)\,\mathbf{Pr}(l) = \mathcal{U}(0, l) \times \mathcal{N}^+(7, 0.1). \tag{38}$$

Thus, the pdf of the prior parameter vector $\mathbf{Pr}(\theta)$ is simply the product of the distributions listed in Table I. With the likelihood and prior pdfs now defined, equation (32) provides the posterior distribution. Note that, even though standard likelihood and prior distributions were assumed, the nonlinear nature of the forward model $v_M(\theta)$ makes the posterior distribution nonstandard (*i.e.*, not Gaussian, uniform, or any other textbook distribution). In fact, the general posterior distribution can be multi-modal, and this fact has important consequences for fault detection. The final subsection provides an example.

TABLE I
PARAMETER PRIOR INFORMATION

| Param. | Distribution | Description |
|---|---|---|
| $l$ | $\mathcal{N}^+(7, 0.1)$ m | cable length |
| $d_F$ | $\mathcal{U}(0, l)$ m | distance to fault |
| $l_F$ | $\mathcal{U}(0, 50)$ mm | fault length |
| $w_F$ | $\mathcal{U}(0, 2b)$ mm | fault width |
| $\epsilon_d$ | $\mathcal{N}^+(2.25, 0.2)$ | relative dielectric permittivity |
| $\sigma_c$ | $\mathcal{N}^+(3, 2) \times 10^7$ S/m | core & shield conductivity |
| $Z_S$ | $\mathcal{N}^+(50, 2)$ $\Omega$ | source impedance |
| $t_M$ | $\mathcal{N}^+(0.5, 0.2)$ ns | measurement time delay |
| $G$ | $\mathcal{N}^+(1, 0.1)$ | system gain |

TABLE II
PARAMETER ESTIMATES $\pm$ 1 STANDARD DEVIATION

| Param. | Estimate | Param. | Estimate |
|---|---|---|---|
| $d_F$ | $6.010 \pm 0.034$ m | $l_F$ | $14.5 \pm 1.9$ mm |
| $w_F$ | $2.71 \pm 0.10$ mm | $\epsilon_d$ | $2.242 \pm 0.025$ |
| $\sigma_c$ | $3.019 \pm 0.008 \times 10^7$ S/m | $Z_S$ | $48.9 \pm 0.3$ $\Omega$ |
| $l$ | $7.02 \pm 0.04$ m | $t_M$ | $0.552 \pm 0.005$ ns |
| $G$ | $0.991 \pm 0.000$ | | |

### B. Chafing Fault Detection Example

As an example, our estimation procedure is applied to the simultaneous retrieval of all parameters from a single measured TDR response collected from a 7-m long RG58 coaxial cable with a single 10 mm $\times$ 3 mm chafe at a distance of 6 m from the source.[5] The optimal estimates are shown in Table II, along with their corresponding standard deviations. Also, Figure 8 characterizes joint estimation performance between pairs of parameters. Note that the correlation between fault width and fault length is expected since changing these parameters in the forward model has roughly the same effect on the TDR response. The model also explains the very strong correlation between the cable length $l$ and dielectric permittivity $\epsilon_d$, since both affect the total propagation time through the cable (*i.e.*, $\epsilon_d$ affects propagation velocity).

Finally, with all the key model parameters inferred from data, we now use the optimal parameter estimates and the known source voltage profile $v_S(t)$ to compute the model-predicted TDR signal, $v_M(t)$. The result presented in Figure 9 shows nearly perfect agreement with the laboratory measurement, thus validating the accuracy of the forward model.

### C. A Multi-modal Example

The example in the previous section highlighted a case where the fault signature was small, but visible by eye. As

[3]In practice, the $\|y - v_M(\theta)\|^2$ term in (36) is computed directly in the frequency domain for each $\theta$ and thus does not require the Fast Fourier Transform operations specified in (23) for each evaluation.

[4]This is necessary to assure that the forward model is not evaluated with non-physical values of its arguments during the Bayesian inference process.

[5]Lab measurements were made using a tape measure for distance to fault and cable length, and digital calipers for fault length and width. These measurements are all subject to some inaccuracy.

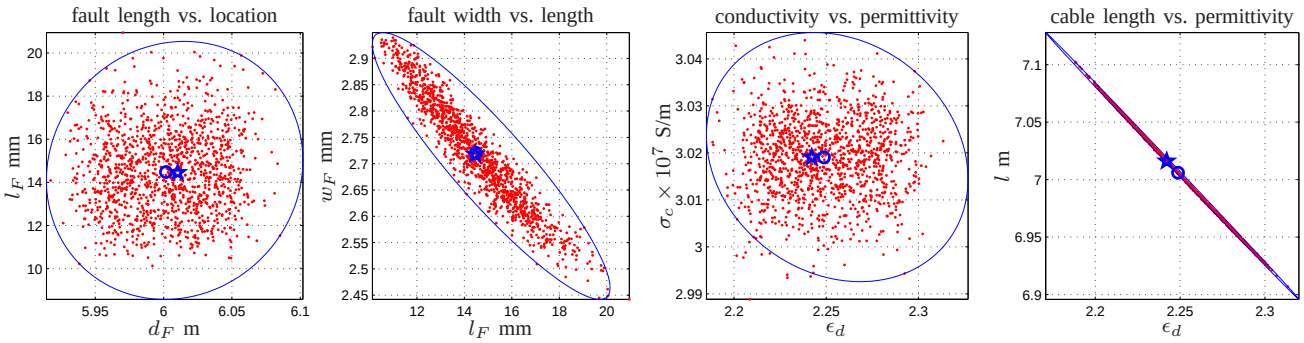


Fig. 8. Example parameter estimation results and uncertainty analysis. The star marks the posterior mode (the most probable estimate) and the circle marks the posterior mean, while the confidence ellipse is the minimum-area ellipse enclosing 95% of the most likely samples from the posterior distribution.

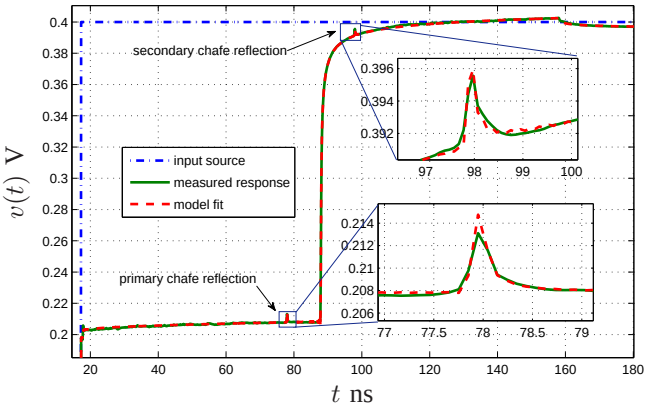


Fig. 9. Model fit to the measured TDR signal using the optimal estimate for $\theta$. The fit captures the variation in the measured signal to within a standard deviation of 0.43 mV, and includes both the primary and the secondary reflections from the chafing fault.

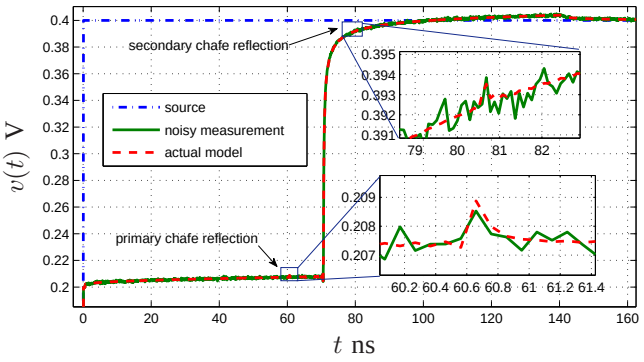


Fig. 10. Actual model for the TDR response to a coaxial cable with a 6 mm $\times$ 2 mm fault, 6 m from the source, and simulated noisy measured data (model plus zero mean Gaussian measurement noise with $\sigma_M = 0.5$ mV). Even though the reflection signature is buried in noise, the maximum posterior estimate correctly characterizes it to the extent shown in Figure 11.

shown in Figure 8, the posterior samples in that case are well modeled by a multivariate Gaussian distribution; and that *is* the standard treatment for a posterior distribution built around general nonlinear models, as in the present case. This approach, however, is not always appropriate. For example, Figure 11 presents the posterior samples from a *simulated* TDR response (again with measurement noise $\sigma_M = 0.5$ mV), to a 6 mm $\times$ 2 mm fault still located 6 m from the source. In this case, the fault signature is buried in the measurement noise (see Figure 10), and the estimation procedure yields posterior samples that cluster around various possible fault locations along the cable. Clearly, these samples are not well described by a multivariate Gaussian distribution, so the standard approach would yield very misleading results. Thus, we can conclude that the standard method is inaccurate for assessing fault detectability at or near the limits of detection.

The MCMC parameter estimation approach presented in this article naturally reveals the proper multi-modal distribution by treating the full nonlinear model without further approximation. In this particular case, Figure 11 shows that the primary mode of the distribution provides good estimates for the fault location and length, but that is not known in advance. Given the available measured data, prior information, and model, one can conclude only that the most likely fault is at 6 m, but other locations are also somewhat probable. In fact, that is just what the posterior samples provide: a set of probable parameter values given the assumed model and measured data.

In closing, we emphasize these examples were selected to highlight the advantages provided by our probabilistic inversion approach using perhaps the simplest possible *realistic* example: the detection of a single chafe in coaxial cable. In other wiring types, particularly non-impedance controlled wire, the situation becomes more complex because changes in impedance, usually caused by changing distance between conductors (or ground plane) with distance, lead to additional reflections that can mask chafing faults, an effect discussed in [3]. Our framework is adaptable to these cases by either parameterizing the effect and thus absorbing it into the model, or by developing a noise model to represent a random (and hence unknowable) change in impedance with distance. While the best way to actually accomplish this is an open research area, the probabilistic inversion approach discussed in this article would still rigorously characterize fault detectability (or un-detectability) in these cases.

## V. Conclusion

This article presented a composite forward model for the TDR response of chafed coaxial cable, given the input signal and a set of model parameters. The novelty in our approach

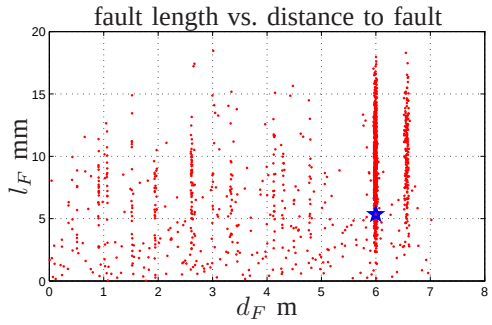


Fig. 11. Fault detection example for a small chafe. In this case, the posterior samples, which represent possible fault locations and lengths, reveal an underlying multi-modal posterior distribution. While the most likely estimate, marked by the star, provides a good estimate of fault location and size, the posterior samples indicate a number of other possibilities that cannot be ruled out given the measured TDR data.

lies not in the application of electromagnetics or $S$-parameter based signal modeling, but in the identification of the important model parameters and system structure needed to accurately represent the actual hardware measured TDR response in the simplest possible way. This was in fact the direct result of a long process of trial and error with lab measured data – a full description of which the reader has been spared. The resulting model incorporates key practical effects such as source–cable impedance mismatch, measurement delay, signal loss and dispersion, changing cable characteristics, and even some degree of mis-calibration. These issues are not specific to the coaxial cable chafe fault detection example this article focused on, and are all important to the general application of TDR-based wiring fault detection methods in the field.

The forward model was then combined with a Bayesian inversion framework to formulate and solve the problem of optimal fault detection and performance characterization using MCMC based techniques. Although this method is computationally slow, it handles general nonlinear models without further approximation; and this leads to an accurate characterization of estimation uncertainty that most traditional methods can fail to provide. Experimental and simulation results highlighted this effect through two simple chafe fault detection examples in coaxial cable. Furthermore, this method is optimal in the sense that, given the measured TDR response, no other detection method can find a more likely fault location and size under equivalent conditions (*i.e.*, same measurement hardware, input signal, noise, wiring system *etc.*).

Finally, the inversion approach is easily generalized to handle a variety of parametric models, since the model itself is viewed simply as an input to the inversion procedure. Thus, we have presented a truly generalized framework applicable to the characterization of TDR-based fault detection for a large variety of TDR hardware, wiring types, and network topologies.

## Appendix
## Nested Sampling

In this appendix we provide a brief summary of the nested sampling algorithm. A complete description can be found in [15], [16], and a more in depth mathematical analysis in [17]. Note, some of the material presented here is supplementary to these references.

To begin, we define the likelihood superlevel set $A_\lambda = \{\theta : \mathbf{Pr}(y|\theta) > \lambda\}$ and associated *prior mass* function

$$\xi(\lambda) = \int_{\theta \in A_\lambda} \mathbf{Pr}(\theta)\, d\theta. \tag{39}$$

Thus, $\xi(\lambda)$ measures the amount of prior probability associated with the likelihood superlevel set $A_\lambda$.

Starting with $n$ samples $\theta_k$, for $k = 1, 2, \ldots, n$, from the prior distribution restricted to $A_\lambda$ (*i.e.*, $\theta_k \sim \mathbf{Pr}(\theta)$ *given* $\theta \in A_\lambda$), the core nested sampling algorithm is:

1) Reject $\theta^* = \operatorname{argmin}_k \mathbf{Pr}(y|\theta_k)$.
2) Set $\lambda^* = \mathbf{Pr}(y|\theta^*)$.
3) Sample one new $\theta_k \sim \mathbf{Pr}(\theta)$ given $\theta \in A_{\lambda^*}$.

The output from this process is then the rejected sample $\theta^*$, and a set of $n$ samples all in the new likelihood superlevel set $A_{\lambda^*} \subset A_\lambda$, since one always has $\lambda^* > \lambda$. Initializing $\lambda$ to zero, the above algorithm is then repeated until a stopping criterion is met, say after $N$ iterations, and $\lambda$ is updated to $\lambda^*$ after each iteration. The net result is then a set of rejected samples $\theta_k^*$ and corresponding likelihood values $\lambda_k^*$ for $k = 1, 2, \ldots, N$. For the results presented in section §IV, we used $n = 300$, and $N \approx 23000$, although $N$ was determined by a stopping criterion based on the numerical progress of the algorithm.

It also turns out [15, Ch. 9] that each rejected sample $\theta_k^*$ corresponds to an unknown random amount of prior mass $\xi_k^* = \xi(\lambda_k^*)$, but with known distribution, such that,

$$\log \xi_k^* = \frac{-k \pm \sqrt{k}}{n}. \tag{40}$$

Thus, *on average*, $\xi_k^* = e^{-k/n}$, and this provides an estimate of the prior probability that $\theta \in A_{\lambda_k^*}$. Now, the sets $B_k = A_{\lambda_k^*} \cap A^c_{\lambda_{k+1}^*}$ for $k = 1, 2, \ldots, N-1$, and $B_N = A_{\lambda_N}$ form a disjoint partition of the sample space $A_0$. Thus, if the likelihood function $\mathbf{Pr}(y|\theta)$ is further assumed approximately constant for all values of $\theta$ in each of these sets[6], one has the following approximation for the evidence integral[7],

$$\begin{aligned} Z &= \int_{\theta \in A_0} \mathbf{Pr}(y|\theta)\, \mathbf{Pr}(\theta)\, d\theta \\ &\approx \sum_{k=1}^{N} \mathbf{Pr}(y|\theta_k^*) \int_{\theta \in B_k} \mathbf{Pr}(\theta)\, d\theta \\ &= \sum_{k=1}^{N} \mathbf{Pr}(y|\theta_k^*)\, \mathbf{Pr}(\theta \in B_k) \\ &\approx \sum_{k=1}^{N} \lambda_k^* h_k, \end{aligned}$$

where $h_k = (\xi_k^* - \xi_{k+1}^*) \approx \mathbf{Pr}(\theta \in B_k)$ for $k = 1, 2, \ldots, N-1$, and $h_N = \xi_N^*$.

At each iteration of the nested sampling algorithm it is required to sample one new value from the prior distribution restricted to a likelihood superlevel set (*i.e.*, step 3).

[6] In fact, for all $\theta$ in each $B_k$ we have that $\lambda_k^* < \mathbf{Pr}(y|\theta) \leq \lambda_{k+1}^*$.

[7] The idea behind this method of calculating the evidence integral is a numerical version of the same basic idea underlying Lebesgue's theory of integration.

A variety of approaches are possible. The easiest way is by rejection sampling: sample values from $\mathbf{Pr}(\theta)$ until one falls into the desired set. This approach however, becomes extremely inefficient once the prior mass associated with the likelihood superlevel sets becomes small (*i.e.*, as the algorithm proceeds the superlevel sets are progressively reduced, and so is the associated prior mass). The approach we took was to use the $n-1$ samples already available from the restricted region to form a multivariate Gaussian proposal distribution at each iteration (using the mean and covariance of the $n-1$ samples). The proposal distribution was then used to obtain the desired new sample using the Metropolis-Hastings algorithm initialized to a sample selected randomly from the $n-1$ samples already available. A *burnin* period was also used to help enhance the independence of each new sample.

The final step is to obtain the posterior samples. So far, we have $N$ samples $\theta_k^*$ each representing a region with posterior mass $(\lambda_k^* h_k)/Z$, for $k = 1, 2, \ldots, N$. Thus, resampling from this collection of *weighted* samples according their posterior masses will yield the desired set of *unweighted* posterior samples (*i.e.*, samples that appear with the correct posterior probability). Following [15, §9.4.2], one can accomplish this in an efficient way that ensures no repeats in the final list of posterior samples.

## REFERENCES


[1] K. R. Wheeler, D. A. Timucin, I. X. Twombly, K. F. Goebel, and P. F. Wysocki, "Aging aircraft wiring fault detection survey," NASA Ames Research Center, http://ti.arc.nasa.gov/m/pub/1342h/1342 (Wheeler).pdf, Tech. Rep. 1342, June 2007.

[2] S. Schuet, D. Timucin, and K. Wheeler, "A model-based probabilistic inversion framework for wire fault detection using tdr," in *Proc. IEEE International Instrumentation and Measurement Technology Conference (I2MTC'10)*, 2010, pp. 422–425.

[3] L. Griffiths, R. Parakh, C. Furse, and B. Baker, "The invisible fray, a critical analysis of the use of reflectometry for fray location," *IEEE Sensors J.*, vol. 6, no. 3, pp. 697–706, June 2006.

[4] E. Song, Y.-J. Shin, P. E. Stone, J. Wang, T.-S. Choe, J.-G. Yook, and J. B. Park, "Detection and location of multiple wiring faults via time-frequency-domain reflectometry," *IEEE Transactions on Electromagnetic Compatability*, vol. 51, no. 1, pp. 131–138, February 2009.

[5] G. Cerri, R. De Leo, L. Della Nebbia, S. Pennesi, V. Primiani, and P. Russo, "Fault location on shielded cables: Electromagnetic modelling and improved measurement data processing," *IEE Proceedings - Science, Measurement and Technology*, vol. 152, no. 5, pp. 217–226, 9 2005.

[6] P. Smith, C. Furse, and J. Gunther, "Analysis of spread spectrum time domain reflectometry for wire fault location," *IEEE Sensors J.*, vol. 5, no. 6, pp. 1469–1478, December 2005.

[7] C. Furse, S. Wu, M. Diamond, D. Mih, C. Lo, and P. Smith, "The potential of prognostics for preventative maintenance of electrical wiring," in *Conference on Aging Aircraft*. FAA and DoD and NASA, April 2007.

[8] C. Furse, Y. Chung, C. Lo, and P. Pendayala, "A critical comparison of reflectometry methods for location of wiring faults," in *Smart Structures and Systems*, 2006, pp. 25–46.

[9] D. Thrimawithana and U. Madawala, "Modeling pulse reflections due to multiple discontinuities on electric fence structures," in *IEEE International Conference on Industrial Technology*, April 2008, pp. 1–6.

[10] I. Platt and I. Woodhead, "Improving the resolution of non-invasive time domain reflectometry," in *3rd International Conference on Sensing Technology*, November 2008, pp. 224–233.

[11] R. Collin, *Foundations for Microwave Engineering*, 2nd ed. New York: McGraw-Hill, Inc., 1992.

[12] R. Ludwig and P. Bretchko, *RF Circuit Design Theory and Applications*. Prentice Hall, 2000.

[13] J. A. Stratton, *Electromagnetic Theory*. New York: McGraw-Hill, 1941.

[14] M. Kowalski, "A simple and efficient computational approach to chafed cable time-domain reflectometry signature prediction," in *Annual Review of Progress in Applied Computational Electromagnetics Conference*. ACES, March 2009.

[15] D. Sivia and D. Skilling, *Data Analysis*, 2nd ed. Oxford University Press, 2006.

[16] J. Skilling, "Nested sampling for general bayesian computation," *Bayesian Analysis*, vol. 1, no. 4, pp. 833–860, 2006. [Online]. Available: http://ba.stat.cmu.edu/journal/2006/vol01/issue04/skilling.pdf

[17] N. Chopin and C. P. Robert, "Properties of nested sampling," *Biometrika*, p. asq021, 2010. [Online]. Available: http://biomet.oxfordjournals.org/cgi/content/abstract/asq021v1


**Stefan Schuet** (M'09) received the B.S. and M.S. degrees in electrical engineering from Santa Clara University, Santa Clara, CA, in 2001 and 2004, respectively. Mr. Stefan Schuet has been a research and development engineer at NASA Ames Research Center since 2001. He is currently working within the Intelligent Systems Division as the project lead for the electromagnetic characterization and detection of wiring faults in avionic systems. He holds a U.S. patent and has won several distinguished awards including the NASA Ames Honor for Excellence in the Engineer Category, NASA Government Invention of the Year Award, and the *R&D Magazine* Top 100 Award.

**Kevin Wheeler** received his B.S. (1988) and M.S. (1991) in electrical engineering from the University of New Hampshire, and his Ph.D. in electrical engineering from the University of Cincinnati (1996) specializing in statistical signal processing. After graduation he joined I.B.M. Almaden Research center to develop web-mining algorithms. He left I.B.M. to work at the Computational Sciences division at NASA Ames Research Center (ARC) in Moffett Field C.A. in 1997. He currently performs research in the Intelligent Systems Division focused upon applying probability theory to automating problems in diagnosis and prognosis.

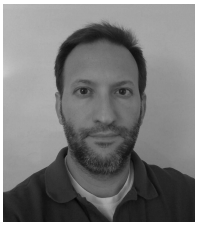

**Doğan Timuçin** holds B.S., M.S., and Ph.D. degrees in electrical engineering, and has been with the NASA Ames Research Center since 1995. He has performed research on holographic optical memories, quantum computing algorithms, radiative transfer models for remote sensing, statistical physics models for air traffic control, and most recently, modeling and inference of faults in electrical wiring and interconnect systems.